npj | flexible electronics

www.nature.com/npjflexelectron

ARTICLE OPEN

Check for updates

A fully inkjet-printed disposable gas sensor matrix with molecularly imprinted gas-selective materials

Lingpu Ge[1], Xiao Ye[1], Zeping Yu[1], Bin Chen[1], Chuanjun Liu[1], Hao Guo[1], Shiyi Zhang[1], Fumihiro Sassa[1] and Kenshi Hayashi[1] ✉

A method was used to fabricate a fully inkjet-printed gas sensor matrix on photographic paper. An electrode matrix comprising 36 interdigital electrodes in a high-density layout that is easy to integrate has been fabricated using a combination of insulating ink and commercial silver ink. Molecular-imprinted polymer (MIP) inks were then made using a simple solution mixing method, and these inks were printed together with carbon black ink on the electrode matrix to complete production of the sensor. Finally, experimental dynamic sensing of volatile organic compounds verifies that for detection of gases corresponding to the MIP template molecules, the MIP layer offers improvements in both sensitivity and selectivity when compared with non-imprinted polymer layers. The matrix can produce a response of more than 20% to 3 ppm propenoic acid gas through adjustment of the printing times for the carbon black layer and the MIP layer.

npj Flexible Electronics (2022)6:40 ; https://doi.org/10.1038/s41528-022-00168-6

INTRODUCTION

Volatile organic compounds (VOCs) exist in the air in indoor and outdoor environments[1]. Long-term exposure to air-containing VOCs will have adverse effects on human health and may cause so-called sick building syndrome[2,3]. In addition, the skin and parts of the human body also produce some VOCs[4]. The production of these VOCs is related to gender, age, genetics, physiological state, and eating habits[5,6]. Therefore, simple but effective VOC monitoring method development, particularly for room temperature VOC monitoring, is important for fields including air quality monitoring, human health monitoring, and medical diagnosis. Traditionally, VOCs have been analyzed via the gas chromatography-mass spectrometry (GC-MS) method[7]. However, because of the disadvantages of GC-MS, e.g., high cost, large volume, and non-real-time analysis, it is necessary to develop sensors to detect organic compounds. Recently, sensors including localized surface plasmon resonance (LSPR) sensors[8], quartz crystal microbalance (QCM) sensors[9], surface acoustic wave sensors[10], and metal oxide sensors[11], were developed for VOC detection.

Chemiresistor-type gas sensors have been widely investigated and used to detect VOCs because of advantages that include cost-effectiveness, a simple sensing mechanism, and easy integration[12]. Their working principle is that when the target gas exists, it can then interact with the sensing material through covalent bonding, hydrogen bonds, or molecular recognition, causing the sensing material's resistance to change[13]. The gas can then be detected by measuring the sensing material resistance. A basic chemiresistor gas sensor comprises a set of interdigital electrodes and a sensing layer that covers the electrodes[14,15]. Common sensing layer fabrication methods include drop coating[16], spin coating[17], screen printing[18], and inkjet printing[19]. Among these methods, the development of chemiresistor gas sensors on flexible substrates using inkjet printing is becoming an important research area[20,21]. This method has attracted extensive attention because this sensor type's advantages include high monitoring sensitivity, light weight, good flexibility, and designability[22,23].

However, VOCs are composed of a complex matrix of chemicals, regardless of whether these VOCs come from air pollutants[24] or various human body parts[25], including low molecular weight fatty acids, aldehydes, alcohols, ketones, ethers, and esters. A single chemiresistor gas sensor is a nonspecific sensor and cannot perform more accurate analyses of VOCs with complex compositions. The use of a molecularly imprinted polymer (MIP) sensitive layer combined with the sensor matrix can solve this problem effectively[26]. This technology can realize selective gas molecule recognition. Molecular imprinting represents an effective approach to create recognition patterns with diverse shapes and sizes for target molecules[27]. MIPs are three-dimensional polymer networks obtained by copolymerization of functional monomers with crosslinkers in the presence of target molecules[28]. When the template molecules are removed from a polymer network by washing or heating, nanoscale cavities similar to the template molecules are generated[29,30]. Using these highly specific cavities, MIPs have been applied as highly selective sensing layers in some gas sensors[31]. When the target molecule exists in the cavity within the three-dimensional polymer structure, it will cause the material's resistance to change; the changes are then measured and converted into observable electrical signals. MIPs are used widely in chemiresistor gas sensors because of their low cost, easy synthesis, stable performance, and reusability[32].

In our work, a stable insulating ink, carbon black (CB) ink and four MIP inks were formulated and were suitable for home printer use. Subsequently, a fully printed flexible gas sensor matrix was fabricated on photographic paper using a home printer. The full sensor-matrix printing process, sensor-matrix specifications, and full sensor unit details are shown in Supplementary Fig. 1. The sensor matrix comprises the following elements:

1. In all, 36 interdigital electrodes that are used to form sensors with sensing layers.
2. In total, 12 silver-based electrodes that connect the interdigital electrodes to the electrical characterization bench; these electrodes are divided into six-row electrodes and six-column electrodes.
3. An acrylic resin insulating layer that electrically insulates the row electrodes from the column electrodes, which are used to perform the measurements.
4. An MIP-based gas-sensitive layer.

[1]Graduate School of Information Science and Electrical Engineering, Kyushu University, 744, Motooka, Nishi-ku, Fukuoka 819-0395, Japan. ✉email: hayashi@ed.kyushu-u.ac.jp

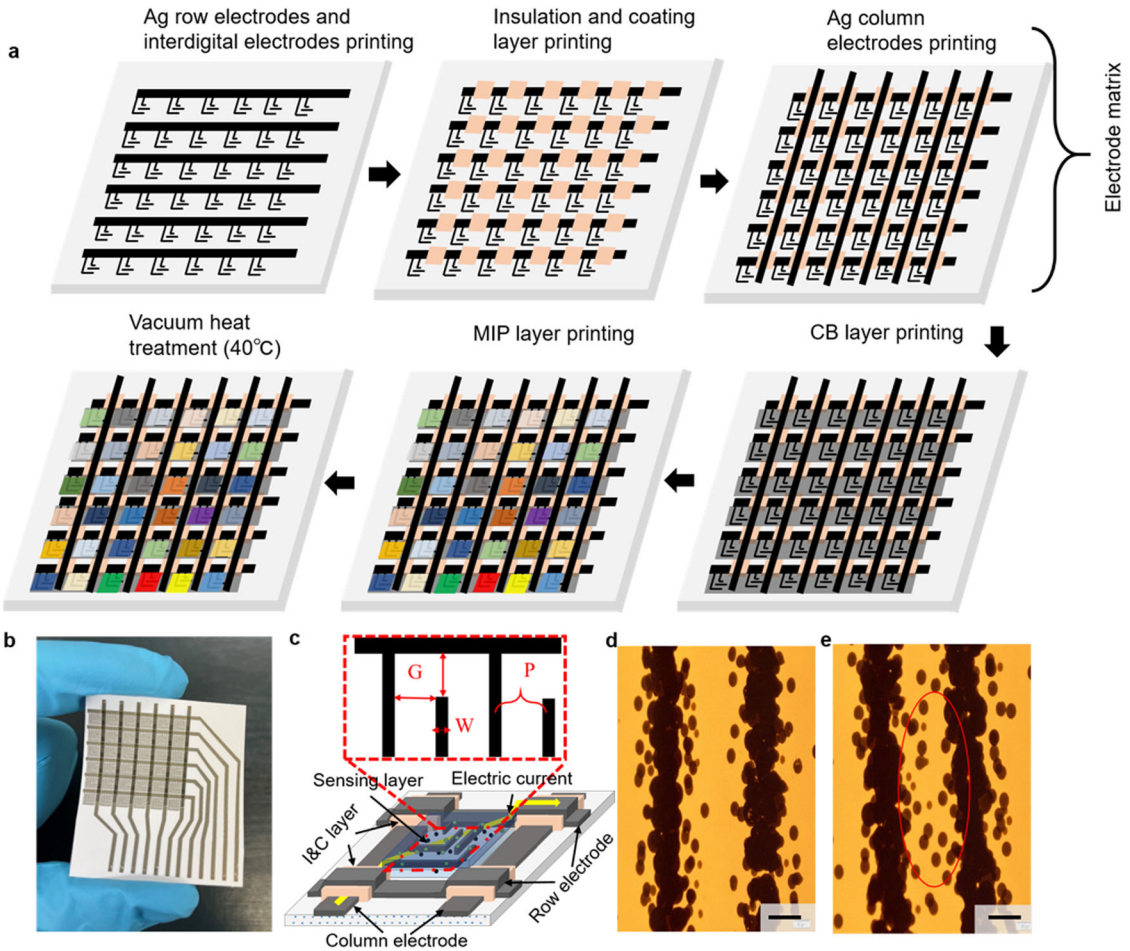

Fig. 1 Printed electrode matrix and sensor matrix. a Schematic of printed sensor-matrix fabrication process. **b** Photograph of the completed sensor matrix. **c** Schematic of the silver interdigital electrode with pitch (*P*), gap (*G*), and width (*W*) parameters. **d** Microscope image of $G = 230\ \mu m$ silver interdigital electrodes. **e** Microscope image of $G = 180\ \mu m$ silver interdigital electrodes and interdigital gap showing evidence of silver ink microsplashing (scale bar = 100 μm).

This stacked structure reduces the number of electrodes required for the measurements significantly and leads to easier sensor integration into an electronic data acquisition card. In addition, in printed electronics, this stacked structure greatly increases the sensor density per unit area when compared with a single-layer sensor array structure.

In this work, we printed acrylic dispersions to produce the insulating layer; this layer can also be used as an ink-absorbing layer by adjusting the film's wettability. Inkjet printing provides a low-cost MIP thin film fabrication method. We prepared four MIP inks using polyacrylic acid (PAA) polymer and four template VOCs (propenoic acid, hexanoic acid, heptanoic acid, and octanoic acid). The CB ink and MIP inks were printed on the surfaces of interdigital electrodes as sensing layers. We studied the printability of these inks and performed physical and electrical characterizations.

Finally, we investigated the responses and sensitivity of the sensor matrix to four gases: propenoic acid, hexanoic acid, heptanoic acid, and octanoic acid. The optimal CB layer and MIP layer printing times were selected via a control variable method. In addition, we also characterize the stability, repeatability, and flexibility of the sensor matrix.

RESULTS

Sensor design

The sensor matrix was designed and printed in a multilayer configuration to embed all sensor elements on the photographic paper. The dimensions of a sensor matrix with 36 sensor units are 36×42 mm. One sheet of A4 photographic paper can produce 30 sensor matrices to this specification. The sensor matrix was fabricated using the following six steps, as shown in Fig. 1a. First, the row electrodes and interdigital electrodes (IDEs) were printed using an inkjet printer with commercially available silver ink. Second, a layer with insulation and coating (I&C) properties is required between the row and column electrodes and is named the I&C layer. This I&C layer is produced by printing a square pattern with a side length of 1.6 mm six times using homemade insulating ink. Third, the column electrodes are printed over the insulating layer and on the photographic paper simultaneously. Fourth, the CB layer is produced by printing CB ink multiple times. The CB layer printing times can be adjusted based on the sensor-matrix requirements. Fifth, the MIP layer is produced on the CB layer using MIP ink. The different colors in the MIP layer in Fig. 1a represent different types of MIP inks, which are the key to achieving gas selectivity. The sensing unit of the gas sensor matrix is composed of interdigital electrodes, CB layer, and MIP layer. The row and column electrodes are respectively connected with the IDEs of each sensing unit, providing an interface for measuring the resistance of it. Sixth, after all printing is completed, the sensor matrix must be vacuum heated at 40 °C for 30 min. This step allows the template molecules in the MIP layer to be removed. A photograph of a completed sensor matrix is shown in Fig. 1b. The main IDE parameters are shown in Fig. 1c. The electrode pitch, gap, and width were 0.3, 0.23, and 0.07 mm, respectively. Studies

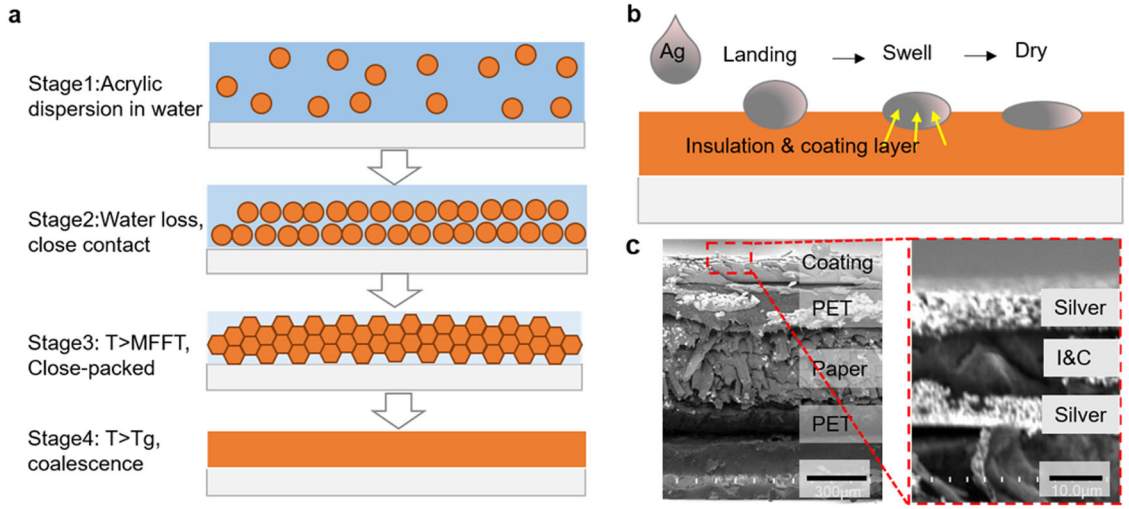

Fig. 2 Microstructure analysis of I&C layer. a Film formation from acrylic dispersions. **b** Principle of ink absorption on the polymer-type coating layer. **c** Cross-sectional scanning electron microscopy (SEM) images of the photographic paper and the I&C layer. Scale bars are 90 μm (left panels) and 30 μm (right panels).

have shown that the sensor's sensitivity can be improved by increasing the density of the IDEs[33]. However, when the distance between the electrodes is too small, micro-splattering of the ink during printing will create microscopic electrical paths between the printed interdigital electrodes and cause short circuits. Under the condition that the interdigital electrode width remains unchanged, printed IDEs with $G = 230$ μm and $G = 180$ μm are shown in Fig. 1d and e, respectively. Obviously, it is more appropriate for the IDE gap to be set at 230 μm.

Preparation of I&C layer by inkjet

In this study, the main component of the insulating ink is an acrylic dispersion. The microscopic I&C layer formation process is also the process of thin-film formation from the acrylic dispersion liquid. Acrylic dispersions generally have high molecular weight, which aids in high-quality film formation. The formation of the acrylic film is mainly divided into four stages[34]. First, the aqueous acrylic dispersion solution is diluted by adding water and ethanol to produce a solution with a viscosity that can be printed. The state of the acrylic dispersion in water is shown in stage 1 in Fig. 2a. After the insulating ink is printed on the paper, evaporation of the water causes the latex solids to be locked together, as shown in state 2 in Fig. 2a. When the external temperature T exceeds the minimum film-forming temperature (MFFT), the acrylic solid particles will become closer together until they generate sufficient deformation pressure to form a hexagonal deformation. When T exceeds the glass transition temperature (T_g), the acrylic particles lose their original form completely and form a more coherent film, as shown in state 4 in Fig. 2a. The coating layer (I&C layer) produced by the insulating ink is a polymer-type layer. After silver ink is printed on this type of layer, it will experience three states, as illustrated in Fig. 2b. First, the silver ink falls on the coating layer, which will then absorb the solvent from the silver ink and swell. Finally, a dry and stable column electrode layer will form when the solvent volatilizes completely. When a cross-section of the photographic paper is observed via scanning electron microscopy (SEM), the photographic paper is found to be divided into four layers. The paper layer is sandwiched between two PET layers, and a coating layer is formed on top of the PET layer to fix the ink. Further enlarged observation of the coating layer on the photographic paper shows that we have fabricated a double-layer silver electrode structure. In this structure, an I&C layer with insulation and ink fixing functions is sandwiched between the silver row and column electrodes, as shown in Fig. 2c. The figure shows that the thicknesses of the silver electrode layers and the I&C layer were 15 and 30 μm, respectively.

Morphology and performance analysis of I&C layer

Experiments have shown that if the I&C layer was fabricated by direct dilution and printing of the MYX-2252 solution (Takamatsu Oil & Fat), the silver electrode printed on the I&C layer surface cannot conduct electricity. As Fig. 3a shows, multiple cracks can be observed on the top silver electrode surface via SEM. This phenomenon can be explained using wettability. When silver ink drops on the I&C layer surface, the liquid will agglomerate on the solid surface because of its poor wettability. When the liquid is completely dry, cracks form. The wettability can be changed by adding polymers to the solution[35]. In this study, equal masses of PEG polymer and M-30 polymer were added to the solution and the silver electrode printed on the I&C layer surface was observed. The observation results are shown in Fig. 3b, c. The comparison shows that the I&C layer fabricated using insulating ink with M-30 has better wettability to the silver ink.

The insulating ink with added M-30 is selected for the relationship experiment between the number of printing times and the insulating effect. With increasing numbers of insulating ink printing times, the resistance and standard deviations of the silver electrodes on the bottom and top layers become increasingly high and the insulation effect improves accordingly, as shown in Fig. 3d. When the insulating ink was printed six times, the resistance of the top and bottom layers reached 765 MΩ, which met the insulation requirements.

Three I&C layer types were fabricated using three different insulating inks. The insulating ink used to fabricate I&C layer1 contained no additional polymers and the insulating inks used to fabricate I&C layer2 and I&C layer3 contained added PEG polymer and added M-30, respectively. Silver electrodes were printed on the surfaces of the three I&C layers and conductivity tests were performed, with results as shown in Fig. 3e. Consistent with the SEM observations, the silver electrode print quality was better on the I&C layer made from insulating ink with added M-30.

During the production of the sensor matrix, the I&C layer was produced by printing six layers of insulating ink with added M-30. After the completion of printing of the top silver electrode on the I&C layer, the resistances of the six top silver electrodes and the six bottom silver electrodes in the sensor matrix were measured. The measurement results are shown in Fig. 3f, and the uniformity of the resistance values for each electrode layer is good. Although

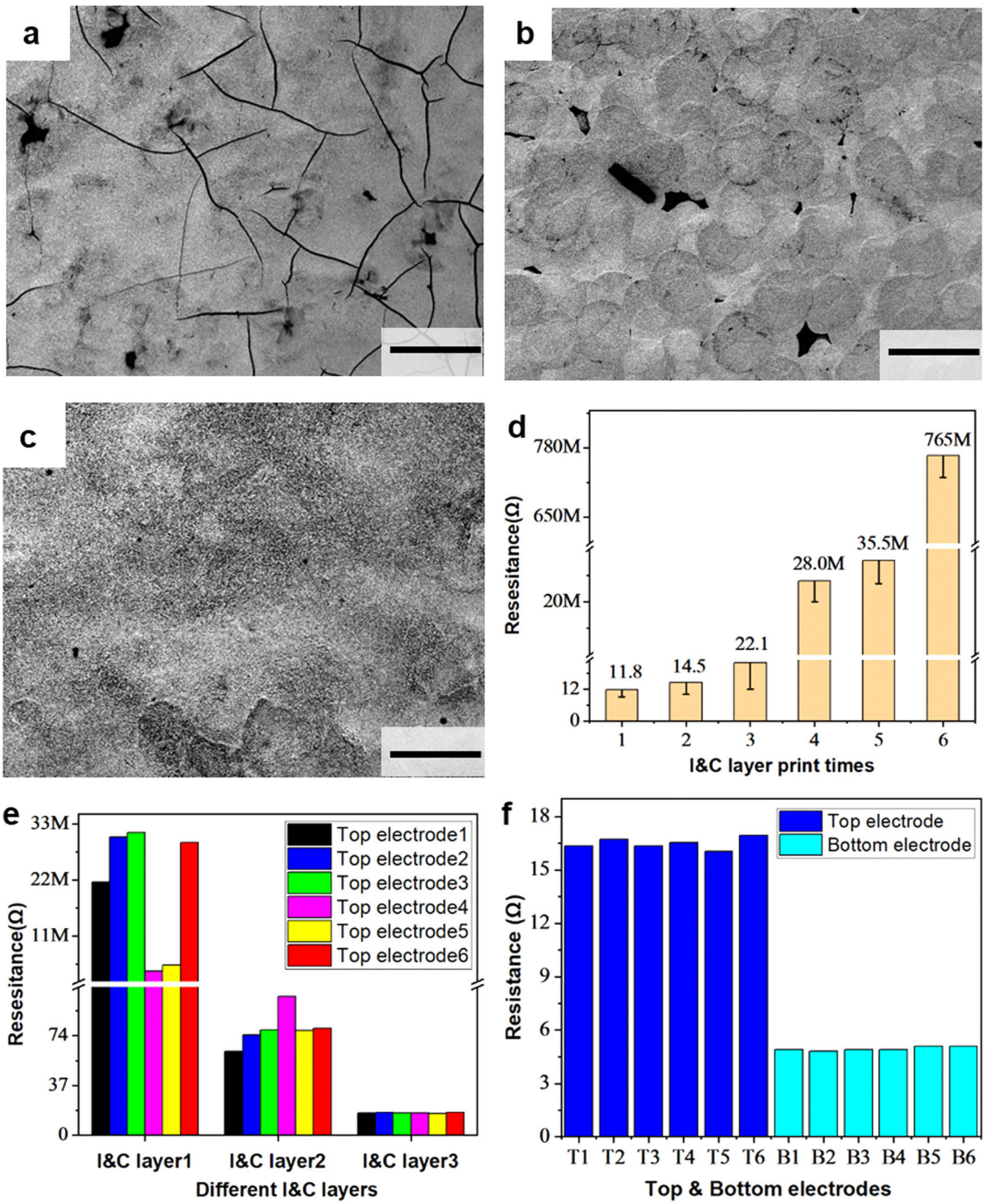

Fig. 3 Insulation and ink fixing functions of I&C layer. SEM images of top (column) silver electrode printing effects, **a** without adding other polymers, **b** with the addition of polyethylene glycol (PEG), and **c** with the addition of M-30 polymer to the insulating ink. **d** Change of resistance between row and column electrodes versus the number of times I&C layers are printed using insulating ink with added M-30. **e** Comparison of resistance values of top silver electrodes printed on three insulating layer types. **f** Comparison of resistance values of the bottom (row) and top (column) silver electrodes of sensor matrix with I&C layers made from insulating ink with added M-30. Scale bars are 30 μm for (**a**–**c**).

the resistance value of the top silver electrode is approximately three times that of the bottom silver electrode, this has no effect on the sensor performance.

Evaluation of organic acid adsorption on MIPs

We prepared four MIP solutions of saturated fatty acids and evaluated the MIP selectivity by the solid-phase microextraction gas chromatography-mass spectrometry (SPME-GC-MS) method. First, we prepared 25 aluminum cups for GC-MS analysis and divided them into five groups: group 1, group 2, group 3, group 4, and group 5. Then, 80 μL of the four MIP and NIP solutions were dropped into the five aluminum cups in each group. Second, aluminum cups containing the same solutions in different groups were placed into a vacuum drying oven in batches and dried at 40 °C for 8 h to remove any organic gas molecules and solvents from the samples completely. Third, after all samples were dried, the GC-MS analysis was performed using the original groups. To

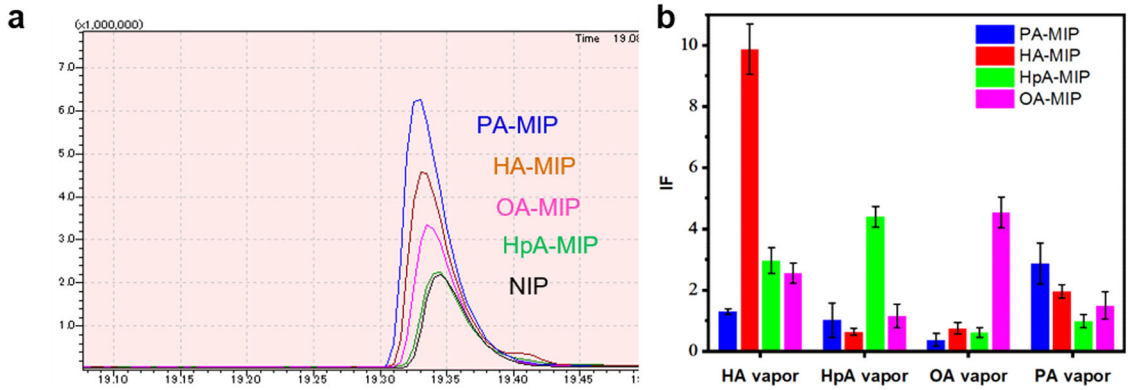

Fig. 4 Selectivity of MIPs. a Gas chromatography-mass spectrometry (GC-MS) results for the four types of MIP when exposed to PA vapors at 100 ppm. **b** Solid-phase microextraction (SPME)-GC-MS results for the four MIP types when exposed to four types of fatty acid vapor (PA/HA/OA/HpA) at 100 ppm.

determine whether the template molecules in the sample could be removed cleanly via vacuum drying, the five samples in group 1 were placed directly into the GC-MS instrument to analyze the residual VOC quantitatively after drying. The use of the similarity search function on the analyzed data showed no significant peak related to the template molecule. Therefore, the VOC in the sample was considered to be removed by vacuum drying. Finally, the SPME-GC-MS method was used to provide quantitative evaluation of the amounts of VOC absorbed by the MIP. The five samples in group 2 were placed in the gas chamber and 100 ppm of propenoic acid (PA) gas was stably flowed for 4 h; the samples were then placed into the GC-MS instrument for analysis. The results are shown in Fig. 4a. The total ion current (TIC) chromatogram shows that the PA-MIP sample has the highest PA vapor absorption. As per group 2, the samples in groups 3, 4, and 5 were flowed with hexanoic acid (HA), heptanoic acid (HpA), and octanoic acid (OA) vapors, respectively, and analyzed using the GC-MS instrument. In each group, the ratio *IF* of the TIC value of each MIP to the NIP was used as a standard to evaluate the amount of VOC absorbed by each MIP, where the normalized VOC absorption $IF = \frac{TIC_{MIP}}{TIC_{NIP}}$. The *IF* values and standard deviations of the four MIPs for absorption of the four VOC gases are shown in Fig. 4b. Analysis of these results shows that the MIP sample has a strong adsorption capacity for the corresponding template molecule, but it also has certain adsorption effects for other gas molecules.

Gas-sensing performance of sensor matrix

CB layers produced using a printer will be more uniform and repeatable. To verify this, we prepared ten sensor matrices and divided them into two groups for experiments. Five sensor matrices with the CB layer produced using a printer were included in the first group and labeled from P1 to P5. Five sensor matrices with a CB layer produced using a micropipette were labeled from M1 to M5. The resistance values of the 36 sensing units for each sensor matrix were measured and the averages and standard deviations were calculated, as shown in Fig. 5a. These results show that the standard deviation of the resistance of the sensor-matrix CB layer in group 1 is much smaller than that in group 2. The CB layer produced using the printer thus has better repeatability. Observation of the CB layer formed by the two methods via an optical microscope shows that the texture of the CB layer fabricated by the printer is more uniform, while there are multiple CB aggregations in the CB layer formed by the micropipette, as shown in Fig. 5b. This phenomenon can be explained as follows: CB aggregation in the solution takes a specific time. Ink droplets printed by the printer are at the picoliter level, while ink droplets produced by the micropipette are at the micrometer level. The CB ink printed by the printer dries more rapidly, thus reducing CB aggregation.

In this study, PA-MIP was used as an example material to select the best CB layer printing times and MIP layer printing times using the controlled variable method. To determine the optimal number of CB layers, six sensor matrices were selected to print the CB layer once, twice, and so on, up to six times. After CB layer printing, each sensor matrix was printed twice with the PA-MIP layer. The average resistance of each sensor matrix and their responses to PA vapor at 6 ppm were measured, as shown in Fig. 5c. As the number of times that the CB layer is printed increases, the resistance value of the sensor matrix decreases accordingly. The response to the gas initially increases and then decreases. Printing of three CB layers produced the best gas response. The reason why the number of CB ink printing times affects the gas response can be explained using the percolation effect. Based on the percolation effect, the CB polymer can be divided into an insulation state, a percolation state, and a conductive state. When the amount of CB in the layer is in the percolation state, the CB polymer's response to the gas reaches a maximum. To determine the best number of MIP layer printing times, we selected six sensor matrices that were printed with three CB layers and with one to six PA-MIP layers for comparison experiments. As shown in Fig. 5d, the gas response intensity was highest when the PA-MIP layer was printed twice. The gas response intensity and speed both decreased gradually with increasing numbers of PA-MIP layers. The gas response principle of this study is that the gas is absorbed by the MIP polymer, thus causing volume expansion and increasing the distance between CB particles. When the direct distance between CB particles increases, the CB layer conductivity decreases and its resistance increases. Therefore, gas detection can be realized by detecting the resistance change. However, with increasing MIP layer thickness, it is increasingly difficult for the microscopic changes in volume after MIP layer gas absorption to affect the CB layer; both the response intensity and response speed will gradually decrease with increasing MIP layer numbers. When only one MIP layer is present, the sensor cannot produce a good gas response because the MIP layer is too thin. In summary, three CB layers plus two MIP layers produce the best response effect.

In a single-sensor matrix, five sensing units were selected for printing of PA-MIP, HA-MIP, HpA-MIP, OA-MIP, and NIP layers. The gas response was tested experimentally using PA gas at 6 ppm as an example, and the experimental results are shown in Fig. 5e. The sensor unit coated with PA-MIP showed the best response to PA gas. Although the NIP layer also responded to PA gas, its response strength was weaker than that of the MIP layer. Finally, HA, HpA, and OA vapors were flowed, and the gas response differences between the printed MIP ink units and the printed NIP ink unit

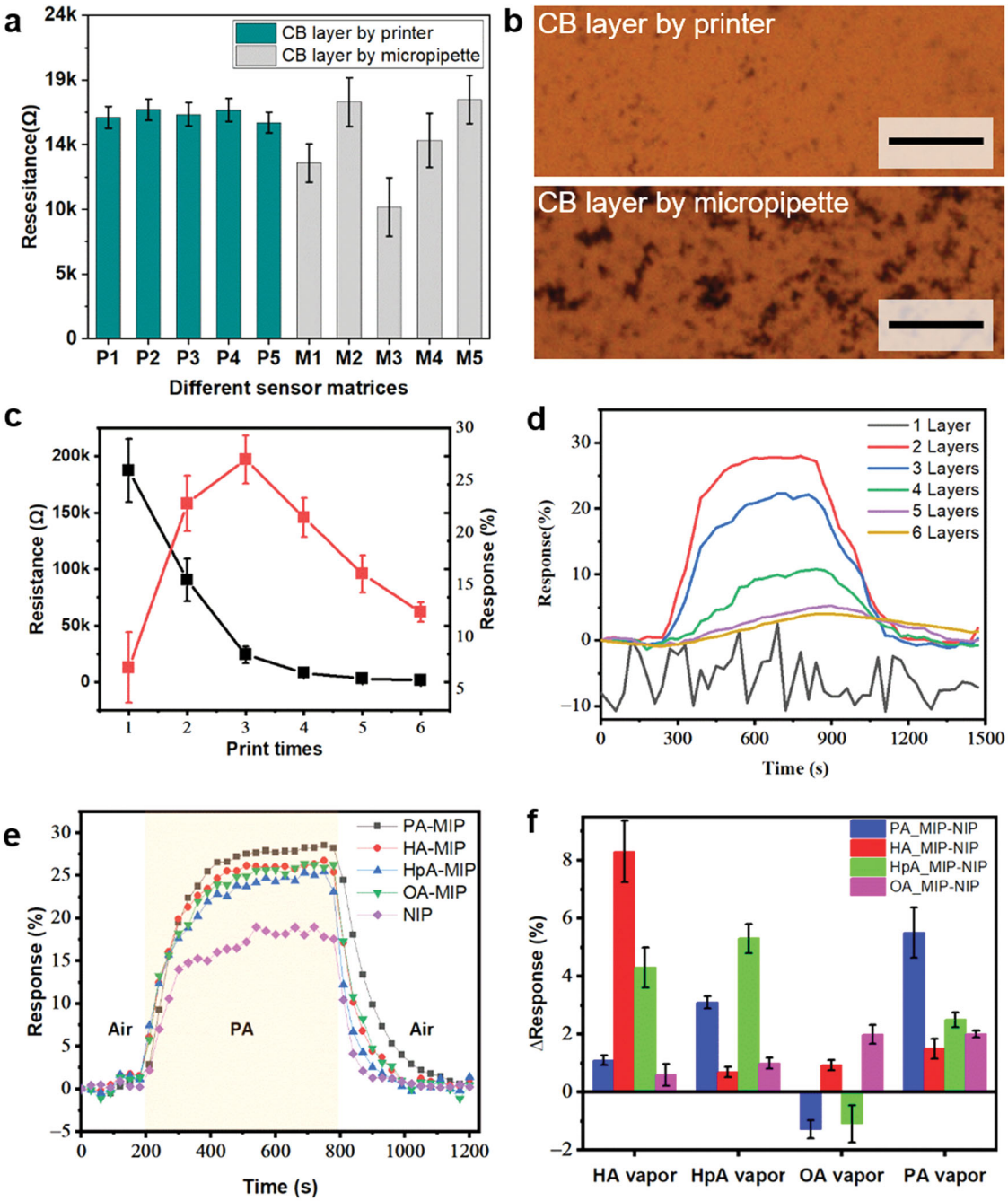

Fig. 5 Uniformity and selective performance of gas sensor matrix. a Average resistances with standard deviations for the different sensor matrices. **b** Micrographs of CB layers (10 μm scale) produced using an inkjet printer and a micropipette. **c** Relationships between number of CB printing times, the average sensor-matrix resistance value, and the response to PA at 6 ppm. **d** Variations in PA sensing response with the number of PA-MIP layers. **e** Real-time responses of sensor units coated with PA-MIP, HA-MIP, HpA-MIP, OA-MIP, and NIP to PA vapor at 6 ppm. **f** Sensitivity of MIP sensor matrix to the same PA, HA, HpA, and OA vapor concentrations.

were used as the normalized response intensities, as shown in Fig. 5f. The experimental results confirm that the MIP layers have the best responses to the VOC vapors, which is consistent with the template molecules.

Response characteristics of sensor unit coated with PA-MIP

The sensor unit printed with PA-MIP ink was used to conduct a gas response characteristic test. Figure 6a shows the sensing characteristics of the sensor unit printed with PA-MIP ink when exposed to PA vapor in a concentration range from 3 to 48 ppm. As the PA vapor concentration increases, the rate of change of the sensor resistance also increases. Detection of unknown PA vapor concentrations can be realized using this positive correlation curve. Figure 6b shows the five-cycle response of the PA-MIP sensing unit when exposed to 3 ppm PA vapor. The experimental results show that the sensor not only has repeatability and recoverability but also can detect relatively low PA vapor concentrations.

The response and recovery characteristics of the sensor unit printed with PA-MIP ink to 3 ppm PA vapor are shown in Fig. 6c. The response time was defined as the time required to reach 80% of the total resistance change after the introduction of the

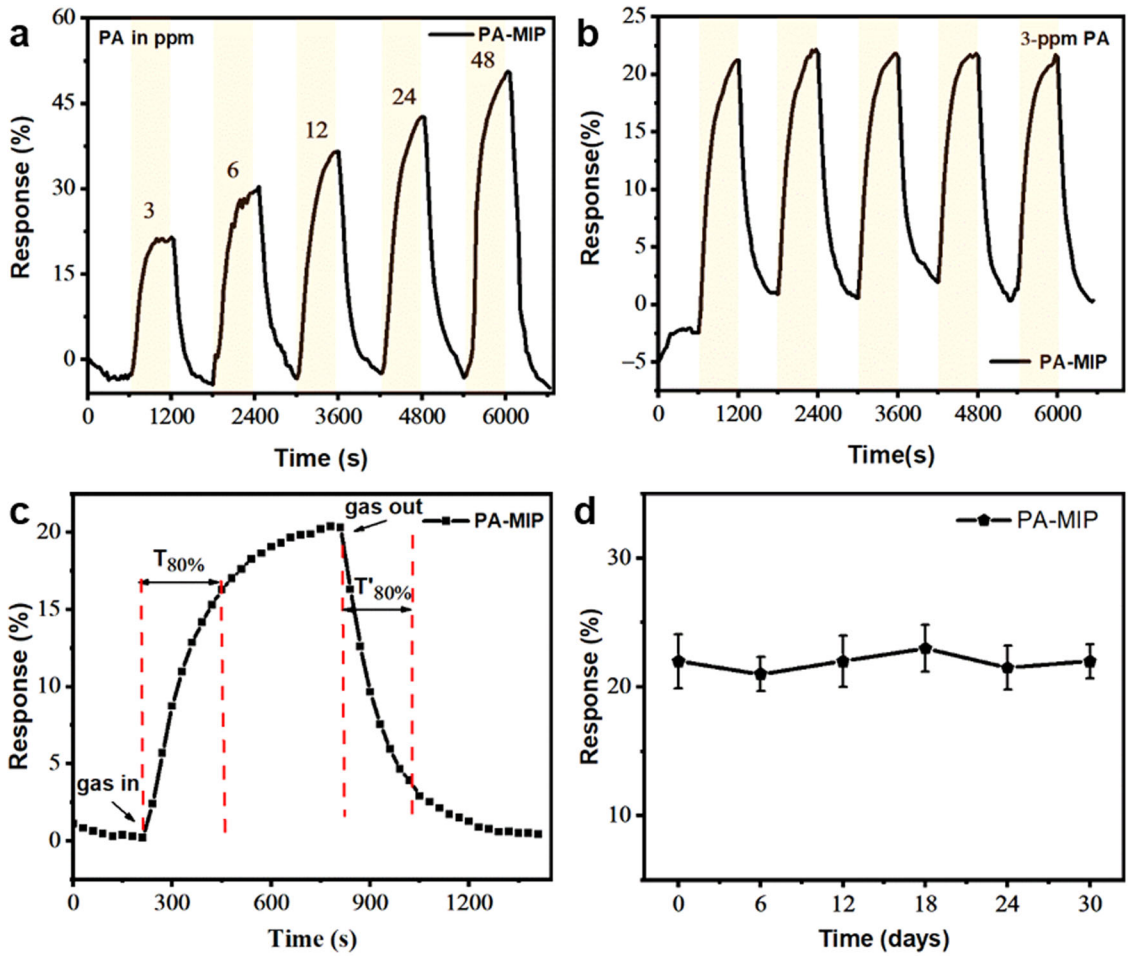

Fig. 6 Response characteristics of sensor unit coated with PA-MIP. a Real-time sensing response of sensor unit coated with PA-MIP to PA vapor exposures at concentrations ranging from 3 to 48 ppm. **b** Cycling performance of sensor unit coated with PA-MIP in response to PA vapor at 3 ppm level. **c** Response and recovery times calculated for 3 ppm of PA. **d** Long-term response stability over one month to 3 ppm of PA for sensor unit coated with PA-MIP.

corresponding organic vapor. The recovery time was defined as the time required to return to 20% of the baseline resistance after removal of the target analyte. Calculations show that the response time $T_{80\%}$ and the recovery time $T'_{80\%}$ for PA vapor are 200 s and 180 s, respectively.

In addition, the sensor matrix was exposed to 3 ppm of PA vapor for one month. During this month, the sensor's gas response intensity was measured by alternately introducing air and 3 ppm PA vapor every 5 days. During this period, the gas response remained stable at ~22.5%, as shown in Fig. 6d. Standard deviations of the measured response values for the ten measurements were only 4.5% at most. The results demonstrate that the sensor matrix shows good long-term stability.

Mechanical stability of MIP-based sensor matrix

Finally, we characterized the fully inkjet-printed flexible sensor using bending tests to evaluate its flexibility and mechanical strength. There is no current uniform standard for the flexibility evaluation of flexible devices. The most common method used for flexible device characterization is cyclic bending testing using a 90° bending angle[36,37]. As Fig. 7a shows, a cyclic bending test was conducted at a bending radius of 5.5 mm at a speed of 100 bends per minute using a customized cyclic translational stage. After every 200 bending tests, the average resistance and standard deviations of each sensor matrix column was measured intermittently, and the results are shown in Fig. 7b. The results show that even after 1000 cycles, the sensor matrix resistance remains quite stable, indicating that the sensor matrix has good flexibility and high mechanical strength. Maintaining this resistance level at the sensor baseline shows that extension of the bending time will not negatively affect the sensing performance of the sensor matrix.

DISCUSSION

In summary, a sensor matrix that can be used to detect different types of VOC has been developed using inkjet printing technology to print inks with differing functions on a low-cost, environmentally friendly, and recyclable photographic paper substrate. The key step in this research lies in the development of functional inks, including CB ink, insulating ink and MIP ink. To improve their printability, the surface tension, viscosity, and other parameters of the different inks have been optimized individually. The film wettability was varied by adding polymers to the acrylic emulsion, allowing the silver electrode to be printed on the I&C layer surface. The gas selectivity of the MIP layer was verified via GC-MS analysis and the gas response method. We expect that the MIP ink production method used in this work will be extended to the development of additional VOC MIP materials. Bending and long-term dynamic sensing tests indicate that the sensor matrix offers good stability and flexibility.

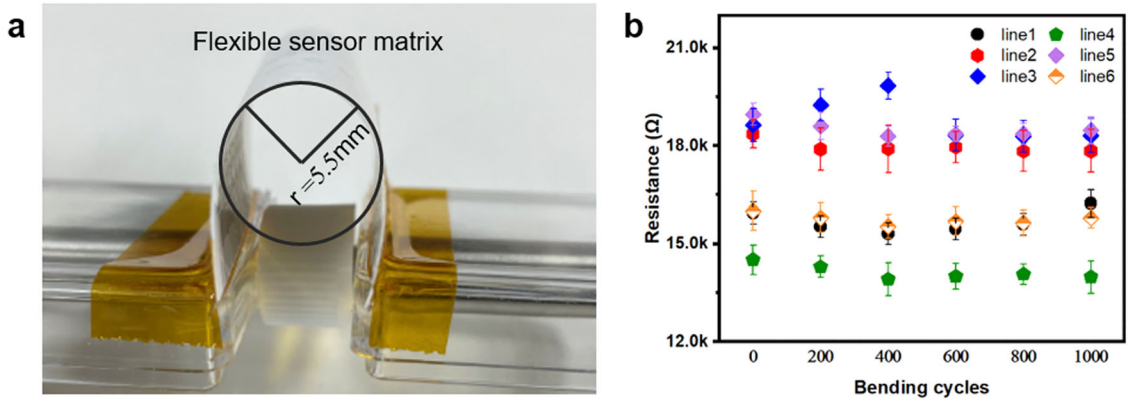

Fig. 7 Characterization of the sensor matrix using bending tests. a Photograph of a flexible sensor matrix. **b** Variations in resistance as a function of the number of bending cycles.

METHODS

Materials

Acetylene CB with a diameter of ~20 nm was used (Strem Chemicals, Newburyport, MA, USA). Ethylene glycol, glycerol, polyoxyethylene (10) octylphenyl ether, poly(acrylic acid) (PAA), propenoic acid, hexanoic acid, heptanoic acid, octanoic acid, and ethanol were all purchased from Fujifilm Wako Pure Chemical. Sodium dodecyl sulfate (SDS) and hydrochloric acid were purchased from Sigma-Aldrich Chemistry. Ethylcellulose was purchased from Tokyo Chemical Industry. Vinyblan 735, a copolymerized resin consisting of vinyl chloride with acrylic acid ester and vinyl acetate, was obtained from Nissin Chemical Industry. MYX-2252 is a type of acrylic resin aqueous dispersion and was received from Takamatsu Oil & Fat Co., Ltd. M-30 is a styrene-maleic acid resin and was obtained from Seiko PMC Corporation. Silver ink (AgIC ink#1000; AgIC, Japan) was poured directly into the cartridge used for inkjet printing. All chemicals were used as received.

Inkjet printer specifications

To perform inkjet printing, we used a commercially available inkjet printer (PX-105, EPSON, Japan) that was equipped with two full sets of refillable ink cartridges (IC4CL69 L, YZQ, Japan). One set of refillable ink cartridges corresponds to four empty cartridges, and these four empty cartridges correspond to the print heads for four colors of ink (black pigment ink, magenta pigment ink, yellow pigment ink, and cyan pigment ink). These refillable ink cartridges were filled with homemade functional inks with adjusted parameters, e.g., viscosity, surface tension, and pH value adjustments, to fabricate the sensor matrix. We used a sheet of A4-sized photographic paper (WPA420PRM, Fujifilm, Japan) to act as a flexible substrate for the sensor and designed the required print patterns using a free vector graphics editor called Inkscape (version 0.91). With regard to the printer's print settings, the paper type and paper quality are the two parameters that must be set. To print out the designed pattern clearly using the corresponding ink, we selected the paper type as *EPSON Photo Matte Paper* and set the quality to *High*.

Preparation of functional inks

Classified in terms of their functions, three types of functional inks had to be made in-house during our research, i.e., CB ink, insulating ink, and the MIP inks. To prepare the CB ink, 5 mg of CB and 100 mg of PAA were added to 9 mL of ethanol. CB can be dispersed more evenly in the ethanol solution as a result of the addition of the PAA polymer. To prevent the nozzle from becoming blocked because of excessively rapid ethanol volatilization during the printing process, we added 0.5 mL of ethylene glycol and 0.5 mL of glycerol to the CB dispersion. 0.1 mL of Vinyblan 735 was added to prevent delamination of the CB layer from the paper. After an ultrasonic water bath treatment for 20 min and filtration through a 5 μm filter, the preparation of the CB ink was complete. To formulate the insulating ink, we prepared a solution comprising 4 mL of water, 2 mL of ethanol, 6 mL of MYX-2252, 50 μL of polyoxyethylene (10) octylphenyl ether, and 300 μL of M-30. Polyoxyethylene (10) octylphenyl ether was used to reduce the surface tension of the ink, and M-30 was used to improve the ink's wettability. Molecular-imprinted polymer inks were prepared using a simple approach via the following four steps. First, four polymer solutions were prepared by dissolving 1 g of PAA in 30 mL of ethanol for each solution. Second, 100 μL of the template molecules were added to the four solutions separately. In this work, propenoic acid, hexanoic acid, heptanoic acid, and octanoic acid were selected as the template molecules. The H bonding between the −COOH group of the target organic acid molecules and the PAA polymer is one of the possible reasons for the adsorption of organic acid gas. Third, 300 μL of hydrochloric acid, 80 mg of SDS, and 50 mg of ethylcellulose were also added to each solution. The addition of ethylcellulose can make the MIP film well fixed on the paper substrate. However, since ethylcellulose is insoluble in water, it is necessary to avoid contact with water during the production and use of the MIP inks. Finally, these solutions were stirred for 4 h to ensure uniform mixing. Non-imprinted polymer inks (NIP inks) were prepared using the same procedure but without the addition of the template molecules. Due to the fast volatilization of ethanol, MIP and NIP inks should be sealed in time during mixing and storage.

Ink characterization

Viscosity and surface tension are important parameters that must be considered to ensure that the ink can be printed using a given printer. The viscosity of the ink was measured using a tuning fork vibration viscometer (SV-10, A&D Co., Japan). The surface tension was measured using the Wilhelmy plate method (DY-300, Kyowa Interface Science, Japan). The basic principle of this method is that when the Wilhelmy plate touches the liquid surface, the liquid will then wet the plate. At this time, the surface tension acts along the periphery of the plate and tries to pull the plate into the liquid. Therefore, the ink surface tension measurement can be completed by measuring the pulling force. The basic parameters for all functional inks are presented in Supplementary Table 1.

Optical microscopy and scanning electron microscopy (SEM)

Micrographs of the CB layers were acquired via optical microscopy (BX53, Olympus, Japan). The surface morphologies of the silver electrodes on the insulating layers were observed via SEM (TM4000Plus, Hitachi, Japan) at an accelerating voltage of 5 kV, a gun current of 6.4 pA and a working distance of 5.6 mm. Cross-sectional images of the photographic paper substrate and the cross-sections of the silver electrodes were acquired using the same SEM. The field emission gun was operated at an accelerating voltage of 5 kV, a gun current of 6.6 pA, and a working distance of 6.6 mm in this case. When the cross-sectional observations were performed, the samples were mounted on a 90° aluminum mount using conductive carbon adhesive tape.

Sensor-matrix testing system

The gas-sensing measurements were performed in a homemade sensor-matrix testing system (Supplementary Fig. 2). This test system can be divided into two parts: the vapor generation system and the measurement system in which the sensor matrix responds to the gas. The vapor generation system consists of an air pump (LV-125A, Lincoln, Japan), an air filter, two mass flow controllers (MFCs; 3660, Kofloc, Japan), a standard gas generator (PD-1B-2, Gastec Corporation, Japan), a three-way solenoid valve

(FSM-0408Y, FLON Industry, Japan) and a gas flow meter (RK 1450, Kofloc, Japan). The air filter is filled with activated carbon, which can be used to dry the air and thus eliminate any influence from water vapor on the gas response. In this study, the MFCs were used to control the carrier gas flow rates, and the three-way solenoid valve was used to control the alternate flows of air and organic gas. The MFCs and the three-way valve were linked to the computer through a NI data acquisition (DAQ; USB-6009, National Instruments, USA) card and then controlled using LabVIEW software. By adding liquids corresponding to the VOC analytes into the diffusion tube in the standard gas generator and setting it at a controlled temperature to maintain stable vapor pressure, the standard concentration of the gas can be produced continuously and stably.

The measurement system consists of a homemade sensor cell, a NI cDAQ-9178 chassis with two C series relay output modules (NI 9485) and a digital multimeter (34110 A, Agilent, USA). The sensor matrix was placed inside a 3D-printed sensor cell with gas inlet and outlet pipelines. The two C series relay output modules were used to select the sensor units of the sensor matrix to be measured. The digital multimeter was used to measure and record the resistance change signal from the sensor unit under test in the sensor matrix.

The response of the sensor matrix is defined as:

$$\text{Response}(\%) = (R - R_0)/R_o \times 100\% \quad (1)$$

where R is the resistance of the sensor matrix in the presence of the VOC analyte, and R_0 is the initial resistance.

DATA AVAILABILITY

The data that support the findings of this study are available from the corresponding author upon request.

Received: 10 September 2021; Accepted: 10 May 2022;
Published online: 07 June 2022

REFERENCES

1. Ohura, T. et al. Comparative study on indoor air quality in Japan and China: characteristics of residential indoor and outdoor VOCs. *Atmos. Environ.* **43**, 6352–6359 (2009).
2. Rostron, J. Sick building syndrome: a review of causes, consequences and remedies. *J. Retail Leis. Prop.* **7**, 291–303 (2008).
3. Chen, W. Y., Yen, C. C., Xue, S., Wang, H. & Stanciu, L. A. Surface functionalization of layered molybdenum disulfide for the selective detection of volatile organic compounds at room temperature. *ACS Appl. Mater. Interfaces* **11**, 34135–34143 (2019).
4. Gallagher, M. et al. Analyses of volatile organic compounds from human skin. *Br. J. Dermatol.* **159**, 780–791 (2008).
5. Shirasu, M. & Touhara, K. The scent of disease: volatile organic compounds of the human body related to disease and disorder. *J. Biochem.* **150**, 257–266 (2011).
6. Mazzatenta, A., Pokorski, M. & Di Giulio, C. Real time analysis of volatile organic compounds (VOCs) in centenarians. *Respir. Physiol. Neurobiol.* **209**, 47–51 (2015).
7. Boots, A. W. et al. Identification of microorganisms based on headspace analysis of volatile organic compounds by gas chromatography-mass spectrometry. *J. Breath. Res.* **8**, 027106 (2014).
8. Shang, L., Liu, C., Watanabe, M., Chen, B. & Hayashi, K. LSPR sensor array based on molecularly imprinted sol-gels for pattern recognition of volatile organic acids. *Sens. Actuators B: Chem.* **249**, 14–21 (2017).
9. Jha, S. K., Liu, C. & Hayashi, K. Molecular imprinted polyacrylic acids based QCM sensor array for recognition of organic acids in body odor. *Sens. Actuators B: Chem.* **204**, 74–87 (2014).
10. Viespe, C. & Grigoriu, C. Surface acoustic wave sensors with carbon nanotubes and SiO2/Si nanoparticles based nanocomposites for VOC detection. *Sens. Actuators B: Chem.* **147**, 43–47 (2010).
11. Marikutsa, A., Novikova, A., Rumyantseva, M., Khmelevsky, N. & Gaskov, A. Comparison of Au-functionalized semiconductor metal oxides in sensitivity to VOC. *Sens. Actuators B: Chem.* **326**, 128980 (2021).
12. Ge, L. et al. Chemiresistor sensor matrix prepared by full-printing processes. *Flex. Print. Electron.* **6**, 015013 (2021).
13. Nazemi, H., Joseph, A., Park, J. & Emadi, A. Advanced micro-and nano-gas sensor technology: a review. *Sensors* **19**, 1285 (2019).
14. Wohltjen, H., Barger, W. R., Snow, A. W. & Jarvis, N. L. Vapor-sensitive chemiresistor fabricated with planar microelectrodes and a Langmuir-Blodgett organic semiconductor film. *IEEE Trans. Electron Devices* **ED-32**, 1170–1174 (1985).
15. Lange, U. & Mirsky, V. M. Chemiresistors based on conducting polymers: a review on measurement techniques. *Anal. Chim. Acta* **687**, 105–113 (2011).
16. Briand, D. et al. Design and fabrication of high-temperature micro-hotplates for drop-coated gas sensors. *Sens. Actuators B: Chem.* **68**, 223–233 (2000).
17. Chen, B. et al. Molecularly imprinted sol-gel/Au@Ag core-shell nano-urchin localized surface plasmon resonance sensor designed in reflection mode for detection of organic acid vapors. *Biosens. Bioelectron.* **169**, 112639 (2020).
18. Moon, S. E. et al. Low power consumption micro C2H5OH gas sensor based on micro-heater and screen printing technique. *Sens. Actuators B: Chem.* **187**, 598–603 (2013).
19. Rieu, M. et al. Fully inkjet printed SnO_2 gas sensor on plastic substrate. *Sens. Actuators B: Chem.* **236**, 1091–1097 (2016).
20. Khan, S. & Briand, D. All-printed low-power metal oxide gas sensors on polymeric substrates. *Flex. Print. Electron.* **4**, 0–8 (2019).
21. Yuan, Y. et al. Convenient CNT-paper gas sensors prepared by a household inkjet printer. *ACS Omega* **5**, 32877–32882 (2020).
22. Mkhize, N., Murugappan, K., Castell, M. R. & Bhaskaran, H. Electrohydrodynamic jet printed conducting polymer for enhanced chemiresistive gas sensors. *J. Mater. Chem. C.* **9**, 4591–4596 (2021).
23. Fioravanti, A. & Carotta, M. C. Year 2020: a snapshot of the last progress in flexible printed gas sensors. *Appl. Sci.* **10**, 1741 (2020).
24. Zhang, X. et al. Characteristics, reactivity and source apportionment of ambient volatile organic compounds (VOCs) in a typical tourist city. *Atmos. Environ.* **215**, 116898 (2019).
25. Drabińska, N. et al. A literature survey of all volatiles from healthy human breath and bodily fluids: the human volatilome. *J. Breath. Res.* **15**, 034001 (2021).
26. Shimizu, K. D. & Stephenson, C. J. Molecularly imprinted polymer sensor arrays. *Curr. Opin. Chem. Biol.* **14**, 743–750 (2010).
27. Janfaza, S. et al. A selective chemiresistive sensor for the cancer-related volatile organic compound hexanal by using molecularly imprinted polymers and multiwalled carbon nanotubes. *Microchim. Acta.* **186**, 137 (2019).
28. Bin, C., Chuanjun, L. & Kenshi, H. Selective terpene vapor detection using molecularly imprinted polymer coated Au nanoparticle LSPR sensor. *IEEE Sens. J.* **14**, 3458–3464 (2014).
29. Hu, Y. et al. The amino-terminal structure of human fragile X mental retardation protein obtained using precipitant-immobilized imprinted polymers. *Nat. Commun.* **6**, 7634 (2015).
30. Vasapollo, G. et al. Molecularly imprinted polymers: Present and future prospective. *Int. J. Mol. Sci.* **12**, 5908–5945 (2011).
31. Belbruno, J. J. Molecularly imprinted polymers. *Chem. Rev.* **119**, 94–119 (2019).
32. Alizadeh, T. & Rezaloo, F. A new chemiresistor sensor based on a blend of carbon nanotube, nano-sized molecularly imprinted polymer and poly methyl methacrylate for the selective and sensitive determination of ethanol vapor. *Sens. Actuators B: Chem.* **176**, 28–37 (2013).
33. Ruth, S. R. A. et al. Flexible fringe effect capacitive sensors with simultaneous high-performance contact and non-contact sensing capabilities. *Small Struct.* **2**, 2000079 (2021).
34. Keddie, J. L., Meredith, P., Jones, R. A. L. & Donald, A. M. Kinetics of film formation in acrylic latices studied with multiple-angle-of-incidence ellipsometry and environmental SEM. *Macromolecules* **28**, 2673–2682 (1995).
35. Li, Z. et al. Microscale effects of polymer on wettability alteration in carbonates. *SPE J.* **25**, 1884–1894 (2020).
36. Chen, W. Y., Jiang, X., Lai, S. N., Peroulis, D. & Stanciu, L. Nanohybrids of a MXene and transition metal dichalcogenide for selective detection of volatile organic compounds. *Nat. Commun.* **11**, 15092 (2020).
37. Trudeau, C., Beaupré, P., Bolduc, M. & Cloutier, S. G. All inkjet-printed perovskite-based bolometers. *npj Flex. Electron.* **4**, 1–5 (2020).

ACKNOWLEDGEMENTS

We are grateful to Takamatsu Oil & Fat Co., Ltd, Seiko PMC Corporation and Nissin Chemical Industry for providing free polymer ink samples for use in the development of our ink. We thank Kunio Tawara from Takamatsu Oil & Fat Co., Ltd for his help and support in the development of the insulating ink. The speed of development of the insulating ink was greatly improved because of his profound understanding and analysis of insulating materials. This work was supported by JST SPRING, Grant Number JPMJSP2136.

AUTHOR CONTRIBUTIONS

All authors contributed to the preparation of this paper. F.S. and K.H. planned and designed the experiments. L.G. and X.Y. carried out all the experiments. S.Z. and Z.Y. helped with the realization of the electronics. L.G., B.C., C.L., and K.H. analyzed the data. L.G., H.G., and X.Y. wrote the paper.

COMPETING INTERESTS

The authors declare no competing interests.

ADDITIONAL INFORMATION

Supplementary information The online version contains supplementary material available at https://doi.org/10.1038/s41528-022-00168-6.

Correspondence and requests for materials should be addressed to Kenshi Hayashi.

Reprints and permission information is available at http://www.nature.com/reprints

Publisher's note Springer Nature remains neutral with regard to jurisdictional claims in published maps and institutional affiliations.

Open Access This article is licensed under a Creative Commons Attribution 4.0 International License, which permits use, sharing, adaptation, distribution and reproduction in any medium or format, as long as you give appropriate credit to the original author(s) and the source, provide a link to the Creative Commons license, and indicate if changes were made. The images or other third party material in this article are included in the article's Creative Commons license, unless indicated otherwise in a credit line to the material. If material is not included in the article's Creative Commons license and your intended use is not permitted by statutory regulation or exceeds the permitted use, you will need to obtain permission directly from the copyright holder. To view a copy of this license, visit http://creativecommons.org/licenses/by/4.0/.

© The Author(s) 2022